Molecular growth paths and dust-particles nucleation precursors in Ar/C2H2 low pressure discharges

Gautier Tetard, Armelle Michau, Swaminathan Prasanna, Jonathan Mougenot, Pascal Brault, Khaled Hassouni

Molecular growth paths and dust-particles nucleation precursors in Ar/C_2H_2 low pressure discharges

G. Tetard[1], A, Michau[1], S. Prasanna[1], J. Mougenot[1], P. Brault[2] and K. Hassouni[1]

[1]Université Sorbonne Paris Nord, Laboratoire des Sciences des Procédés et des Matériaux, LSPM, CNRS, UPR 3407, F-93430, Villetaneuse, France
[2]GREMI CNRS—Université d'Orléans, BP744 Orléans Cedex 2, France

Abstract

A numerical model was used to investigate the effect of acetylene concentration in the feed gas on molecular growth and solid particle nucleation in argon-acetylene CCRF discharges. Results showed that for large acetylene conversion yields and small acetylene concentrations in the discharge, the ionization kinetic is driven by Penning process and the molecular growth is governed by neutral polyynes. The cluster size distribution predicted shows that nucleation is unlikely in this situation. On the opposite, for limited conversion yields and significant acetylene concentrations in the discharge, the ionization kinetic is driven by electron-impact process; the molecular growth is governed by positive ions and leads to significant concentrations of neutral polyynes and enhanced nucleation rate.

I. Introduction

Hydrocarbon containing plasmas have been the subject of a large research effort due to the possibilities they offer for the elaboration of functional nanostructures and coatings needed in a variety of advanced applications [1; 2 ; 3-5]. In particular, argon-acetylene plasmas generated in Parallel Plate Capacitively Coupled Radiofrequency (PPCC-RF) discharges were considered since more than 4 decades for the deposition of functional polymeric barrier coatings [6; 7]. These plasmas are however known to favor the formation of amorphous hydrogenated carbon dust particles in the gas phase [8]. Such effects may be highly undesirable when continuous non porous functional coatings are targeted, e.g., for diffusion barrier applications [3]. However it may be of interest in applications where functional nanostructures are targeted. Such nanostructures can be indeed produced by gas phase polymerization in argon acetylene plasmas [9]. This last phenomenon received a strong interest from the scientific community and a large number of studies were indeed devoted to the investigation and the understanding of nanoparticles formation and dusty plasma effects in PPCC-RF argon-acetylene plasmas. In particular, first contributions from Doyle [10] and Stoykov et al. [11] followed by numerical 1D modelling studies [12-15] were carried out in order to investigate pure acetylene CCRF plasmas. Few years later, some efforts were also devoted to the investigation of Ar/C_2H_2 plasmas that present some peculiarities due to the presence of argon metastable, denoted Ar* in the following, that induces an enhanced Penning ionization and dissociation of hydrocarbon molecules thus affecting the plasma polymerization process [16], [17] [18] [19; 20].

However to our best knowledge only few analysis of the molecular growth phase that leads to the nucleation has been performed. An analytical model by Lin et al [21] suggests that negative species should be responsible for the particle nucleation in Ar/C_2H_2 CCRF plasma where the electrostatic trapping of these species enhances their residence time and therefore enables their molecular growth. This proposed nucleation pathway is similar to the one generally invoked in the case of Silane plasmas [22]. Nevertheless, De Bleeker et al [12] and Mao et al [14] concluded that the negative ion pathway is probably dominant owing to the electrostatic trapping of negatively charged ions in the plasmas. It is however worthy to mention that, De Bleeker et al [12] suggested that in addition to the negative ions reaction pathway, an alternative pathway involving positive ions may also effectively contribute towards the production of large hydrocarbon species in pure C_2H_2 plasmas.

Despite the many encouraging results they obtained, all these authors emphasized the need for further investigations in order to assess the dominant nucleation (plasma polymerization) route in hydrocarbon (HC) plasmas [23]. In particular, the conclusions of most of the studies on molecular growth mechanisms in HC plasma are based on the comparison between the population of large negative, positive and neutral HC species. Although such comparisons indicate the nature of the species that may lead to the nucleation, they do not provide concrete conclusions on the molecular growth routes that lead to the dominant species. In other words, large hydrocarbon population dominated by negative ions doesn't necessarily mean that the negative ions are the drivers for the plasma polymerization process.

In this paper, we have focused on the investigation of the molecular growth stage that controls the solid particle nucleation. We especially analyze the molecular growth pathways leading to the nucleation as function of the acetylene content in the feed gas. For this purpose, we have used a one-dimensional self-consistent numerical fluid model of argon-acetylene plasmas [24]. This model has been used to determine the discharge characteristics as well as the concentrations of large hydrocarbon species produced in the plasma as function of the feed gas composition. A detailed analysis of the production routes of these species has been performed. We particularly show that the gas phase molecular growth model used in this study cannot explain nanoparticle nucleation when acetylene conversion yield is large and acetylene concentration in the discharge is low[16]. This may indicate that the plasma/surface interaction could play a major role, in nanoparticle formation observed under low acetylene concentration in argon-acetylene plasmas. When acetylene conversion yield remains limited and acetylene concentration in the discharge significant, the formation of large hydrocarbon species is significantly enhanced, the molecular growth is driven by positive ions although large size hydrocarbon population is dominated by neutral species and the model used here fully explains dust particles nucleation through gas phase molecular growth process.

In the next section a brief presentation of the fluid model used in this study will be given, with a detailed discussion on the kinetic schemes and more particularly on the molecular growth processes leading to the gas phase nucleation of dust particles. We will also discuss the boundary conditions used in the model and their impact on the plasma composition and the subsequent molecular growth kinetics. In section 3, we will present the investigation of the molecular growth and

nucleation kinetics using the one dimensional discharge fluid model along with a chemical model that takes into account up to 20 carbon containing species. We have concentrated on the effects of the gas composition on the discharge behavior and the nucleation kinetics. Then, a detailed analysis of the molecular growth mechanisms in Ar/C_2H_2 plasma at low and high C_2H_2% in the feed gas will be presented. Finally, we analyze the impact of the assumption made on the interaction of the positive ions, that turn out to be the drivers for the molecular growth, with the electrode surface on the plasma behavior and the plasma polymerization kinetics.

II. Model description

The details of the modeling procedure used in this study are discussed in [24]. We make use of a numerical model that couples a discharge dynamic model, a large characteristic time scale transport/chemistry model and a flow transport model [24]. The discharge dynamic model enables simulating the electron dynamic over short time scales, typically much less than the RF period. It especially provides the time-space variation of the electron density and temperature along with the resulting time-averaged electron impact reaction rates. These rates are used in a large characteristic time module in order to simulate the time-variation of the plasma composition over time scales that are much longer than the RF period. The flow model is used to compute the space profile of the flow velocity in the frame of the stagnation line flow theory. Actually the full plasma simulation requires an iterative procedure where these three modules are coupled [24]. At each iteration step, the discharge dynamic is first calculated for a given plasma composition by time-integrating the discharge model equations for several hundreds of RF periods until a periodic behavior of the discharge is obtained. Then using the time-averaged electron impact reaction rates inferred from this discharge model, the coupled flow equation and the long characteristic time continuity equations for chemical species are solved over much longer time scales (typically 1 s). The obtained plasma composition is used to simulate new discharge dynamic and the procedure is iterated until stable plasma composition and electron dynamics are obtained [24].

This simulation procedure enables one overcoming the time stiffness characteristic of Ar/C_2H_2 plasma that involves interdependent very fast electron dynamics processes and a very slow chemistry. It also enables taking into account the flow effect that may be a key-factor in affecting the plasma composition and the discharge dynamic [24]. Below, we briefly describe each of the three modules included in our model.

II. 1. Discharge dynamic model

The discharge module is a fluid model that makes used of the drift/diffusion assumption when solving for the ions and the electron continuity equations:

$$\rho \frac{dY_s}{dt} = -\frac{d\Gamma_s}{dx} + S_s + F_s \tag{1}$$

Where ρ denote the plasma density, while $Y_s, \Gamma_s \; and \; S_s$ represent the species 's' mass fraction, flux density and chemical source term, respectively. The term F_s that appears when taking into account gas flow effects includes a convective flux divergence term and a source term corresponding to the radial convective losses that characterize stagnation line flows [24].

These equations are coupled with the following electron average-energy equation:

$$\frac{d}{dt}(n_e\varepsilon_e) = -\frac{d\Gamma_{\varepsilon e}}{dx} + S_{\varepsilon e} - eE\Gamma_{\varepsilon e} \tag{2}$$

Where n_e, ε_e and $\Gamma_{\varepsilon e}$ represent the electron density, average-energy, and enthalpy flux, respectively. *E* is the electric field and $S_{\varepsilon e}$ the energy loss rate through collisional processes. Note that electron impact reaction rate constants required for estimating $S_{\varepsilon e}$ and S_s are calculated assuming that the electron energy distribution function is solution of the two-term expansion of the electron Boltzmann equation. The self-consistent electric field, *E*, is obtained using Poisson's equation (quasi-static assumption).

II. 2. Large characteristic time transport/chemistry module

In this module, we consider the long term variations of neutral as well as ionic species over time-scales that are much longer than the RF period. The considered equations are derived by time-averaging the species continuity equations over one RF period [24]. These may be expressed as:

$$\rho\frac{dY_s}{dt} = -\frac{d(\mu_s < E >_{T_{RF}} - D_s\frac{dn_s}{dx})}{dx} + < S_e >_{T_{RF}} + S_s + F_s \tag{3}$$

The transport coefficients μ_s and D_s denote the mobility coefficient for charged species and the diffusion coefficient, respectively. The species considered in equation (3) show transport and chemistry characteristic-times that are much longer than the RF period so as their mass fractions, diffusion fluxes and source term components that do not involve electrons, i.e., S_s and F_s, do not vary over RF time scale e.g. $< Y_s >_{T_{RF}} (t) \approx Y_s$.

On the contrary, the local drift fluxes and electron-impact source term components strongly depend on the time-variations of the electron density and temperature that are characterized by a very fast dynamic. These termstherefore needs to be time-averaged. The drift flux is obtained from the time-averaged electric field and corresponds to the DC component of the field, i.e. $\langle E_s\rangle_{T_{RF}} = \langle E\rangle_{T_{RF}} = -\frac{dV_{DC}}{dx}$. The time averaged electron impact component of the source term is calculated in the discharge dynamic module [24].

II. 3. Flow transport model

The feed gas is introduced using a showerhead electrode which is approximated by a porous body in our model. A purely axial flow emerges from this electrode (the left one in figure 1) and is directed toward the facing electrode. Due to the resulting stagnation flow configuration, the flow exits radially outside the gap region. The flow regime has been discussed in [24] where we compared results assuming stagnation line theory flow and two Continuously Stirred Tank Reactor (CSTR) models corresponding to two asymptotic values of the discharge volume to the reactor volume ratios, i.e. $\delta = \frac{V_D}{V_R} \rightarrow 0$ or $\frac{V_D}{V_R} \rightarrow 1$. We showed that, for the considered reactor geometry, the CSTR $\delta\rightarrow 1$ model and the stagnation line theory give similar results for flowrate values below 20 sccm as far as hydrocarbon species are concerned. In this study, we make use of the stagnation line flow model proposed by Coltrin et al [25].

II. 4. Chemistry model for Ar/C_2H_2 plasmas

The chemistry model consists of two sets of reactions. A first one includes primary reactions involving small chemical species such as H_2, C_2H_2 and Ar. It especially describes the ionization and dissociation of the major stable neutral species found in the investigated discharge and the subsequent formation of small radicals and ions. At the gas temperature that characterizes such discharges (300-400 K), the molecular growth essentially involves polyyne molecules, radicals and ions as shown by mass spectrometry measurements in [26], [27] and [28]. As a matter of fact, the Hydrogen Abstraction Carbon Addition (HACA) mechanism widely used in the combustion [29] and also previously investigated for higher temperature microwave plasmas cannot be activated under such low gas temperature conditions [30]. Therefore, the second set of reactions includes molecular growth reactions, ionization and electron-attachment on large polyynes ($C_{2n}H_2$), as well as mutual neutralization of large positive and negative polyyne ions.

Table I: List of chemical species considered in the model

Molecules	Ions	Radicals
Ar	Ar^+	Ar*, H
C_2H_2	$C_2H_2^+$, C_2H^+, C_2H^-	C_2H, C_2, CH_2, CH, C
H_2	H_2^+	H
C_4H_2	$C_4H_2^+$, C_4H^-	C_4H, C_4H_3
C_6H_2	$C_6H_2^+$, $C_6H_4^+$, C_6H^-	C_6H, C_6H_3
C_8H_2	$C_8H_2^+$, $C_8H_6^+$, C_8H^-	C_8H
$C_{2n}H_2$, 2n>8	$C_{2n}H_2^+$, $C_{2n}H_6^+$, $C_{2n}H^-$, 2n>8	$C_{2n}H$, 2n>8

a- Primary plasma reaction model

The chemistry model used in this work is based, with few improvements and an additional set of reactions due to the presence of argon, on the one developed by [14] for pure acetylene plasmas. The model includes electron-impact reactions on argon and his metastable Ar* [31], H_2 [31] and C_2H_2 [32]. These reactions generate small positive ions, i.e., Ar^+, H_2^+, C_2H^+, $C_2H_2^+$, small radicals, i.e., C, C_2, CH, CH_2, C_2H and C_2H^- negative ion. Ar* quenching by reaction with HC species, especially C_2H_2, and leading to ionization and dissociation have also been included. The key-role of these quenching reactions, especially Penning ionization, has been underlined by Stefanovic [16], [33]. Collisional processes leading to electron energy dissipation through vibrational and electronic excitations of C_2H_2 and H_2 are also considered.

b- Molecular growth model

Along with C_2H_2, the small radicals and ions produced by the first set of reactions initiate a molecular growth process. At the ambient temperature characterizing the investigated discharges, one may distinguish two neutral, (R1) and (R2) [34], one negative (R3) [35] and one positive (R4) [36] growth channels. These may be represented as follows:

Table II: Molecular growth process considered in low temperature argon-acetylene plasmas

Process	Rate constant($m^3.mol^{-1}.s^{-1}$)	#
$C_2H + C_{2n}H_2 \rightarrow C_{2n+2}H_2 + H$	3.10^7	(R1)
$C_2H_2 + C_{2n}H \rightarrow C_{2n+2}H_2 + H$	4.10^7	(R2)
$C_2H_2 + C_{2n}H^- \rightarrow C_{2n+2}H^- + H_2$	6.10^5	(R3)

$C_2H_2 + C_{2n}H_y^+ \rightarrow C_{2n+2}H_y^+ + H_2$, (n>2,y=6) 6.10^7 (R4)

It appears that C_2H and C_2H_2 would probably play a key-role in the molecular growth process. It also appears that the growth process will produce an excess of hydrogen in the plasma. At the low temperature discharge considered here, i.e. 300 K, molecular hydrogen can be hardly activated and its interaction with polyyne molecules was not considered. Note however that such interaction cannot be excluded even the stable molecules for high gas temperatures. Such conditions are not investigated in the present work. On the other hand, atomic hydrogen which may react with polyyne even at low temperature shows fairy low concentration. Its effect was not taken into account in agreement with the mass spectra measured on the investigated discharges and which shows that the major species are by far $C_{2n}H_2$ polyynes and their radicals $C_{2n}H$. The three molecular growth channels of Table II are coupled by: (i) radiative and dissociative attachment processes on polyynes [37], (ii) polyyne ionization processes [16]and (iii) mutual neutralization of large polyyne positive and negative ions [38]. One may also notice that neutral and positive-ion reaction channels show much larger reaction rate than the negative ones.

From the practical point of view, the molecular growth can be only described up to a priori prescribed carbon atom numbers which defines the largest molecular edifice in the simulation. In this work we discuss two molecular growth models. The first one considers HC clusters up to 8 carbon atoms. In this case the fate of polyynes larger than $C_8H_{p=1-2}$ is not described by the model. Therefore, the calculated $C_8H_{p=1-2}$ molecules would actually represents all the $C_{2n}H_{p=1-2}$ molecules with $2n \geq 8$.

The second molecular growth model, discussed in section III.2.b, describes polyyne growth up to 20 carbon atoms, i.e., $C_{20}H_{p=1-2}$. This model allows describing the kinetic and predicting the detailed size distribution of polyyne molecules with up to 2n=18 carbon atoms.

II. 5. Boundary conditions

The boundary conditions specified for neutral species are similar to those used by De Bleeker et al. [12]. Stable neutral species are assumed to not react with the surface and are therefore reflected in the gas phase. Radicalar species may either recombine on- or stick to the surface. As far as sticking processes are concerned, we used the reaction-probability values γ proposed by Von Keudell [39], i.e. 0.01 for H, 0.8 for large $C_{2n}H$ radicals and 1 for small radicals such as C, C_2, CH, except CH_2 which is less reactive and for which we used a sticking coefficient value of 0.26. A surface recombination reaction probability value of 10^{-3} was used for HC reactions with H atom adsorbed at the surface, as recommended by Von Keudell [39]. A total de-excitation of Ar* at the electrode is assumed [40].

As far as positive-ions are concerned, we assumed that Ar^+ totally recombines on the surface to produce Ar. The situation is different for HC molecular ions for which two kinds of surface interactions have been suggested in the literature. The first one assumes a total adsorption of the ion impinging on the surface [12]. In this case, the ions contribute to a film growth on the electrode. The second one assumes a total dissociative recombination of the ions with the electrons at the metallic electrode surface [41]. In this case ion recombination takes place through an Auger mechanism where the ion is neutralized by capturing an electron from the surface [42]. The excess energy carried by the produced neutral leads to its dissociation and contributes to the emission of radicals in the gas phase. In principle, the predominant surface recombination reactions for hydrocarbon ions are of (R5) type. However, mass spectrometry measurements ([27],[26]) have shown that $C_{2n}H_2$ and $C_{2n}H$ species are by far the most abundant species among the $C_{2n}H_p$. Therefore, only $C_{2n}H_2$ and $C_{2n}H$ neutral species were taken into account in the chemistry model. As a result, (R5) type surface recombination reactions could only be written for $C_{2n}H_2^+$ ions. For other ions, such as $C_{2n}H_4^+$ or $C_{2n}H_6^+$, the surface recombination reactions were supposed to preserve the number of carbon and lead to the most abundant $C_{2n}H_2$ clusters, the hydrogen balance being insured by H_2 molecule. Therefore,

the surface recombination reactions (R5 bis) and (R5 ter) are used in the model for $C_{2n}H_4^+$ or $C_{2n}H_6^+$, respectively.

$$C_{2n}H_2^+ + wall(e^-) \rightarrow C_{2n}H + H \quad (R5)$$
$$C_6H_4^+ + wall(e^-) \rightarrow C_6H_2 + H_2 \quad (R5\ bis)$$
$$C_{2n}H_6^+ + wall(e^-) \rightarrow C_{2n}H_2 + 2H_2 \quad (R5\ ter)$$

Actually the ion-surface interaction may have a major impact on the plasma composition and can affect molecular growth and particle formation in the gas phase. Therefore the two kinds of boundary conditions discussed above, *i.e.,* full absorption and full recombination, and that probably represent two idealized asymptotic situations will be investigated in this work.

Negative species do not interact with the surface as they are trapped in the bulk of the discharge. Boundary conditions for electron density and temperature are detailed in [24].

Table III: Recombination, sticking and neutralization coefficients for the surface reactions

	Recombination	Sticking	Neutralization	References
Ar^+			1	[40]
Ar*	1			[40]
C, C_2, CH	0	1		[39]
CH_2	10^{-3}	0.26		[39]
$C_{2n}H$	10^{-3}	0.8		[39]
$C_{2n}H_3$	10^{-3}	0.3		[39]
H	0.1	10^{-2}		[39]
$C_{2n}H_y^+$			1	[41]

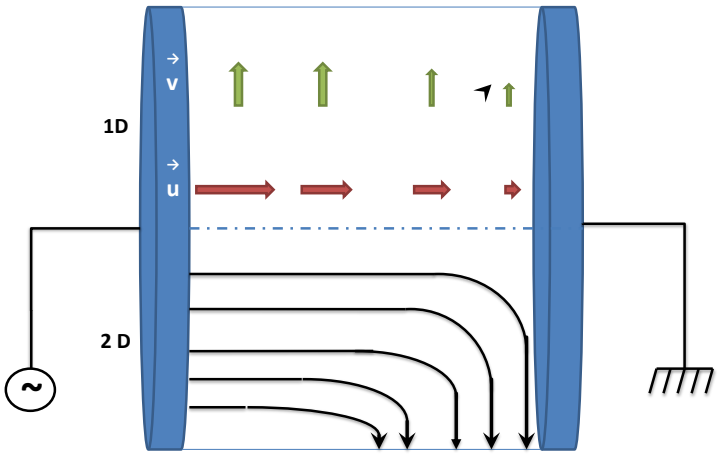

Figure 1: schematic of the investigated reactor geometry showing the shower head electrode and the stagnation line flow

III. Results and discussion

The model described in the previous section was previously evaluated through qualitative comparison with experiments [24]. In this paper we mainly focus on the investigation of molecular growth kinetics in argon acetylene capacitively coupled RF plasma as function of the amount of C_2H_2 in the feed gas (C_2H_2%) for a showerhead electrode feed gas injection configuration. The simulations

are carried out for a 2.54 cm gap distance, 10 Pa pressure, a constant gas temperature of 300K [27], 100 V RF voltage amplitude and 20 cm diameter electrode. The Ar/C_2H_2 mixture is introduced at a flowrate of 20 sccm, which corresponds to an inlet gas velocity of 0.1 m/s and a residence time of 7 s. The C_2H_2 percentage in the feed gas mixture was varied between 1 and 99 %. We first discuss the main characteristics of the discharge, and then analyze the different routes of the molecular growth and subsequent nucleation kinetics as a function of C_2H_2% in the feed gas.

III. 1. Discharge characteristics

Figure **2** shows the time-averaged electron density profiles in the gap for six values of C_2H_2% in the feed gas: 4, 10, 17, 25, 50 and 99%**.** The electron density in the center of the gap shows a first twofold increase when C_2H_2% increases from 4 to 17 % and then decreases by almost 1 order of magnitude, from 2.3 $10^{15}m^{-3}$ to 2.9$10^{14}m^{-3}$, when C_2H_2% is further increased to 99%.

Up to 10% C_2H_2 in the feed gas, the increase of the electron density is due to the increase of C_2H_2 in the gap and a subsequent enhancement of the ionization by Ar* quenching, i.e. Penning ionization, and electron impact. In this range of C_2H_2% the ionization kinetic is limited by the C_2H_2 mole fraction in the gap. When C_2H_2% further increases above 10%, the Penning ionization starts decreasing although it remains the dominant ionization route up to 17% acetylene in the feed gas. Above 17% of C_2H_2, the ionization regime is dominated by electron impact on C_2H_2. The overall ionization rate increases with C_2H_2% up to 17 % of C_2H_2 in the feed gas and then remains almost constant, which does not explain the observed decrease of electron density above 17% C_2H_2 in the feed gas (cf. figure 2 (a)). Actually, a detailed rate analysis shows that this decrease is due to the enhancement of the attachment process kinetics on C_2H_2 and large neutral polyynes when C_2H_2% increases.

The time-averaged axial profiles of the electron temperature show almost constant values except in the sheath where it slightly increases, i.e., 1 eV increase [24] over all the investigated range of C_2H_2%. Its bulk value decreases from 4.7 eV to 3.4 eV when C_2H_2% increases from 4 to 99(figure 2(b)). This behavior is due to the enhanced collisional energy dissipation at larger C_2H_2 concentration in the gap [24].

The power coupled to the plasma varies significantly with C_2H_2% as may be seen in Figure 3(a) that depicts the axial profile of the time-averaged absorbed RF power density ($W.m^{-3}$) in the gap. The power density first slightly increases with C_2H_2% in the range 4-10 % acetylene in the feed gas and then steadily and significantly decreases when C_2H_2% is further increased. Typically, the space-time averaged power density inferred from figure 3(a) and depicted in figure 3(b) shows almost fourfold decrease when C_2H_2% is varied from 10% to 99%. This corresponds to a power decrease from 4 to 1.5 W for 20 cm diameter electrodes (Figure 3(b)).

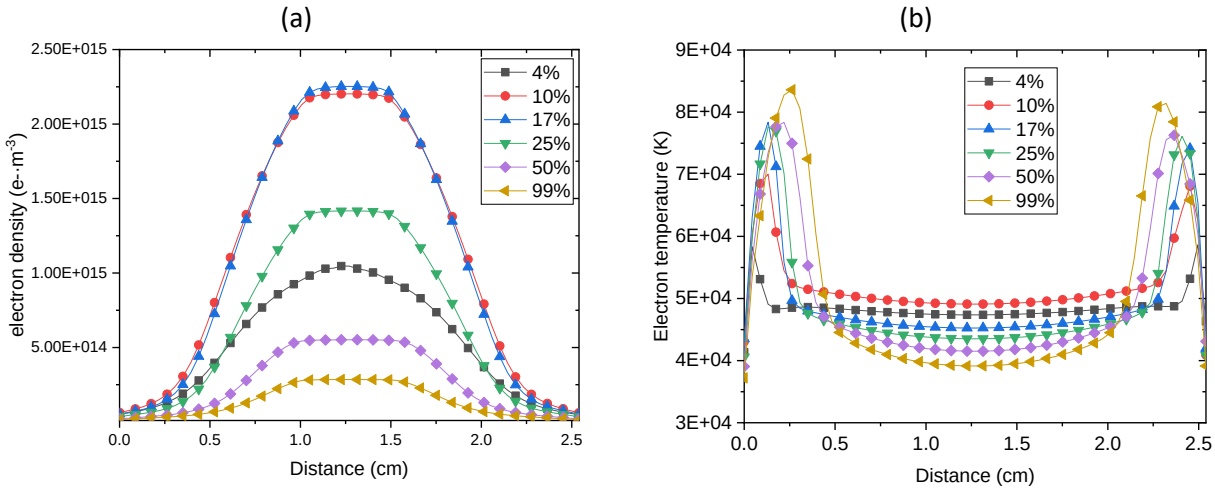

Figure 2: Axial profiles of (a) time-average electron density and (b) time-average electron temperature for different values of C_2H_2%

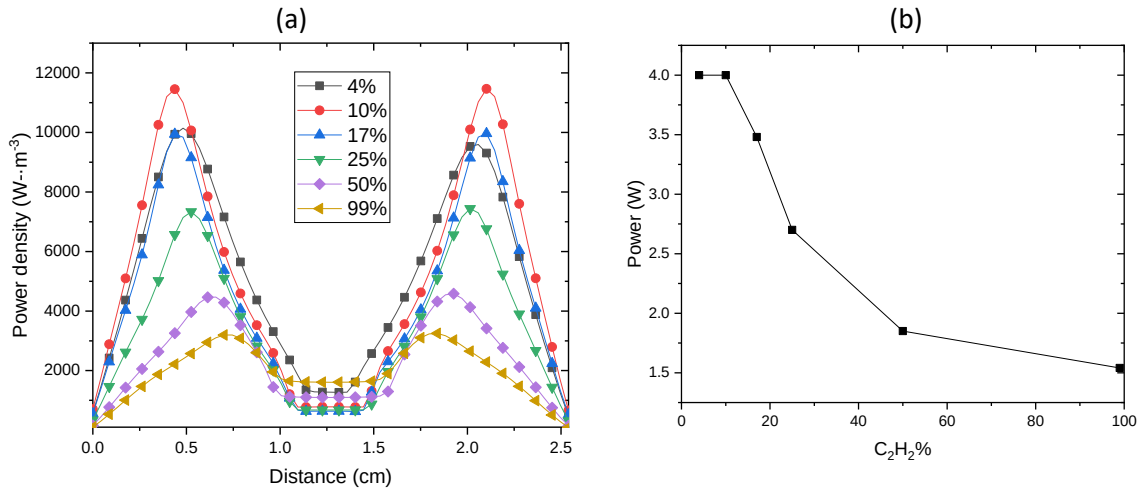

Figure 3: (a) Axial profiles of the time-averaged absorbed RF power density. (b) absorbed RF power as function of C_2H_2%

The acetylene mole fraction does almost not vary with the position in the discharge gap. Figure 4 shows the variation of this mole-fraction as a function of C_2H_2% in the feed gas. We observe that C_2H_2 concentration in the gap is much lower than in the feed gas for C_2H_2% below 25%, while these two concentrations are very close for large C_2H_2%. As a result the conversion yield of C_2H_2 decreases from almost 100% to 10% when increasing C_2H_2% from 4% to 99%, cf. figure 5. The evolution of the C_2H_2 conversion rate as a function of C_2H_2% in the feed gas is depicted in figure 5. This rate shows a maximum for 17 % acetylene in the feed gas, which means that increasing C_2H_2% above this value, does not enhance C_2H_2 conversion. The high conversion yields of acetylene obtained at low C_2H_2% were also observed experimentally [43] [44] [16] and predicted numerically [45] for similar discharges conditions by other groups. The primary fragmentation of C_2H_2 results in C_2H as a major

radicalar species. As shown in figure 4, the concentration of C_2H at the center of the gap strongly decreases when increasing C_2H_2% above 10%. This is due to an almost 5 orders of magnitude decrease in the concentration of Ar*, the quenching of which governs the acetylene fragmentation kinetics at low C_2H_2% [24]. As a result, electron-impact dissociation/ionization processes become dominant and lead, due the decrease of n_e and T_e with C_2H_2%, to a much less effective fragmentation kinetics at high C_2H_2%, i.e., above 17% for the investigated discharge configuration.

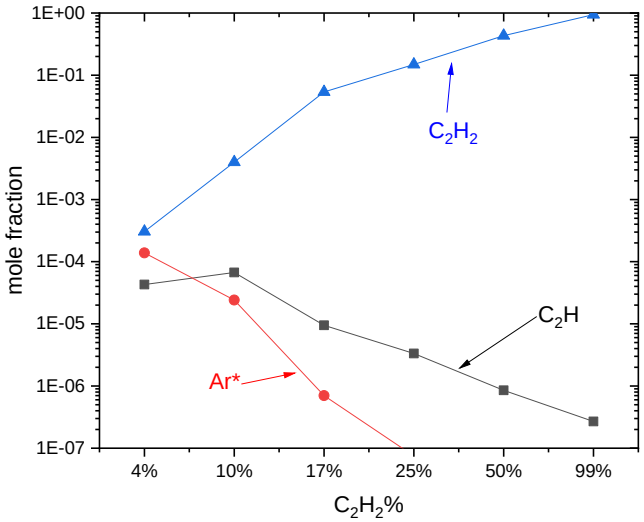

Figure 4: Mole fraction of C_2H_2, C_2H radical and Ar* at the center of the gap as a function of C_2H_2% in the feed gas

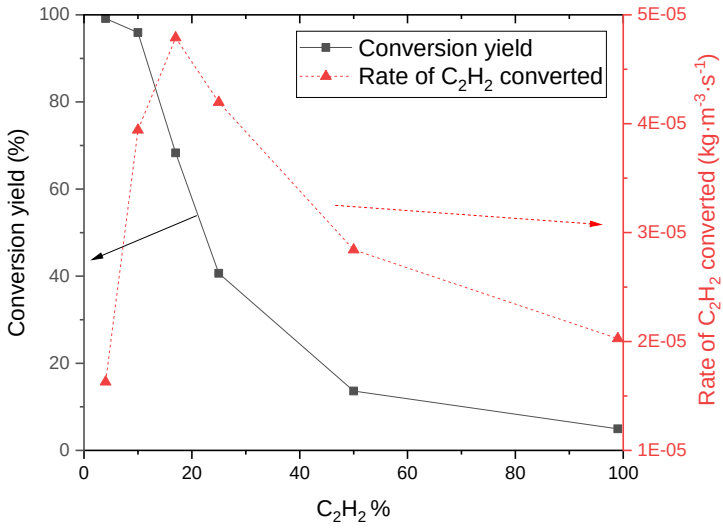

Figure 5: Acetylene conversion yield and rate of C_2H_2 converted as a function of C_2H_2%.

Figure 6(a) shows the molar fraction of negative ions in the bulk of the plasma as a function of C_2H_2%. For 4% C_2H_2 in the feed gas, the discharge is dominated by large negative ions, the production of

which is governed by radiative attachment: $C_{2n}H + e^- \rightarrow C_{2n}H^- + h\nu$. C_2H^- density is very low for this value of C_2H_2%. At larger C_2H_2%, the density of C_2H^- becomes significant although the discharge is still dominated by large negative ions. This is due to the strong increase of acetylene concentrations in the, i. e., more than 3 orders of magnitude increase, when C_2H_2 varies from 4% to 25%. As a result the dissociative attachment on C_2H_2 is substantially enhanced thus favoring C_2H^- production as compared to larger negative ions produced by molecular growth as will be discussed later in section III.2.

When C_2H_2% increases, the discharge evolves from an electropositive to two-region plasma. The first one is a narrow highly electronegative region located at the very center of the gap. The second region is electropositive and surrounds the first one. A very sharp decrease of the negative ion density unambiguously defines the frontier between these two regions (cf. figure 6(b)). Figure 7 shows the axial profiles of the plasma electronegativity α defined as the ratio of the negative ion density to the electron density for different values of C_2H_2%. It appears that the electronegativity maximum located at the center of the gap increases from 1.7 to 44 when C_2H_2% is varied from 4% to 99%.

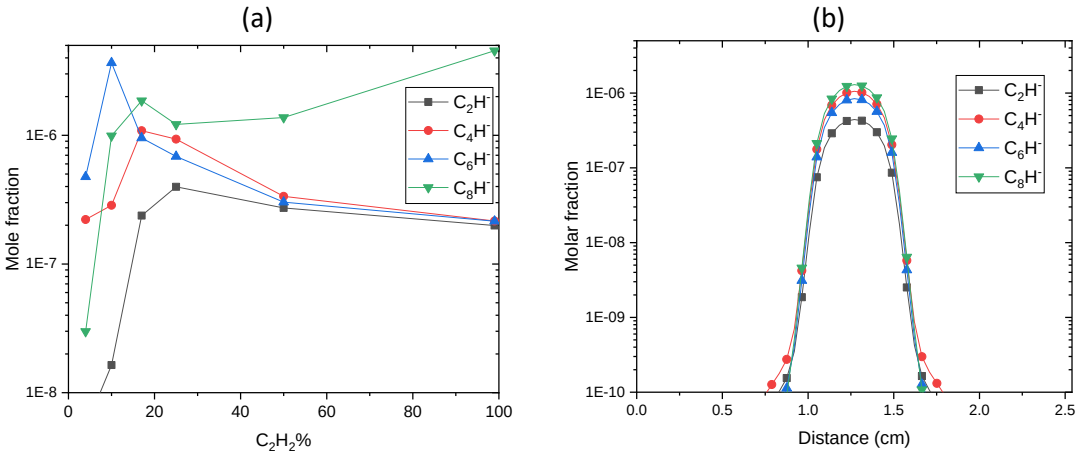

Figure 6: (a) Molar fractions of the negative ions in the bulk as function of C_2H_2%. (b) time-averaged axial distributions of the negative ions for C_2H_2%=25

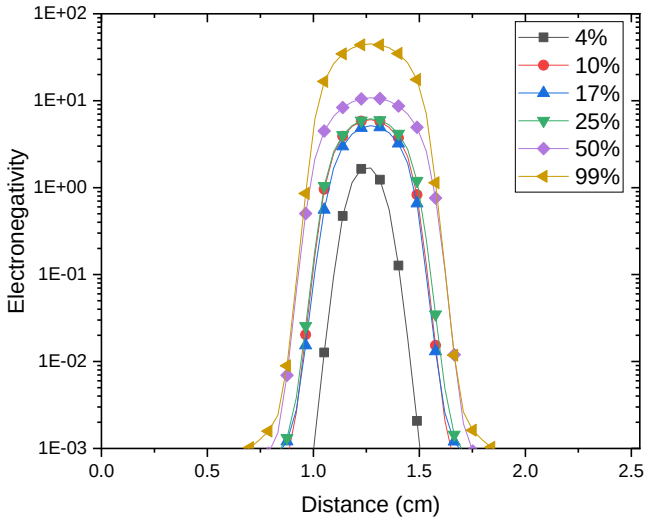

Figure 7 Time-averaged axial distributions of the plasma electronegativity for different values of C_2H_2%

As far as positive ion distributions in the gap are concerned, one may distinguish three types of discharge conditions (cf. figure 8 (a)). At low C_2H_2%, i.e. 4%, the major ions in the whole gap are Ar^+ and $C_2H_2^+$. The ionization kinetic is governed by electron-impact on Ar and C_2H_2 on one hand, and Ar* quenching by hydrocarbon molecules on the other hand (Penning ionization). At intermediate C_2H_2%, i. e. 10%-17%, Ar^+ mole-fraction experiences a strong decrease and the major ions become $C_2H_2^+$ and $C_4H_2^+$ that are produced by Ar* quenching. At larger C_2H_2%, i.e., above 17-25%, $C_2H_2^+$ and $C_4H_2^+$ experience large decreases in the center of the gap where the dominant ion becomes $C_6H_4^+$ which is produced by molecular growth of $C_4H_2^+$. Note however that both $C_2H_2^+$ and $C_6H_4^+$ remain dominant outside the central region of the gap, as may be clearly seen in figure 8 (b) that shows that the axial profiles of positive ions. These present prominent maxima in the electronegative region at the center of the gap. The shape of these profiles results from the negative ion density built-up in the center of the gap. Indeed, once produced, the negative ions drift toward the potential maximum located at the center of the gap. Due to space charge field effect, the negative ions attract the positive ones that are essentially produced at the sheath edges and take them towards the center of the gap so as to insure an ambipolar equilibrium, i.e. ambipolar diffusion effect. The prominent maxima are the results of the balances between the ion fluxes directed from the sheath edge to the center and the mutual recombination processes in the very narrow central electronegative region. In this this region that extends over 8 mm in the gap, the positive and negative ions mole fractions are almost the same, i.e 310^{-6} at 50% of C_2H_2, the electron mole fraction being much lower, i.e 210^{-7}.

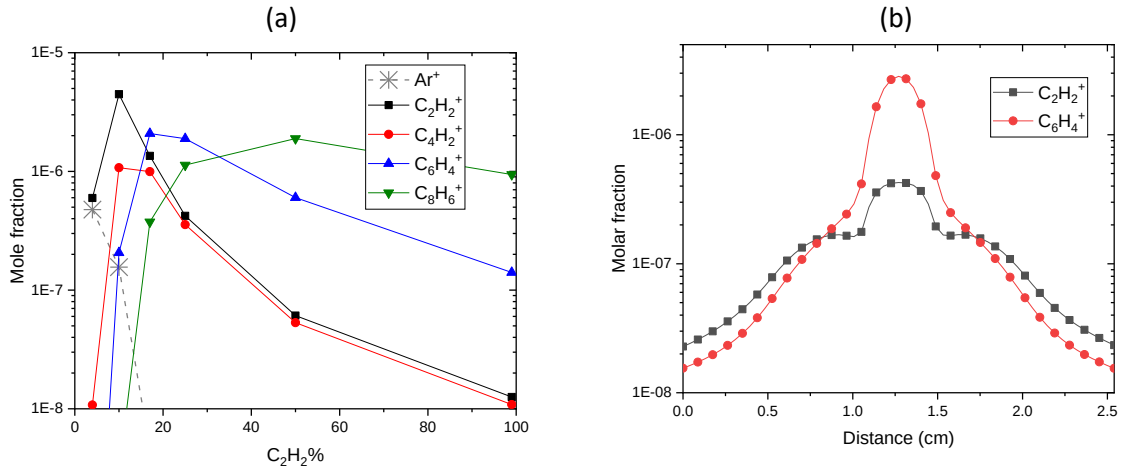

Figure 8 (a) Molar fractions of the positive ions in the center of the gap as function of the %C2H2 and (b) time-averaged axial distributions of C2H2+ and C6H4+ at 25% of C2H2

Figure 9 shows the mole-fractions of the $C_{2n}H_2$ neutral polyynes as functions of C_2H_2% in the bulk of the discharge. $C_{2n}H$ radicals show much smaller concentration and are not represented in the figure. For C_2H_2% above 10%, the major neutral species are C_4H_2, C_6H_2 and C_8H_2 with mole fraction values as high as 10^{-2} for a 50% C_2H_2 feed gas composition. This is three orders of magnitude larger than the charged species mole fractions. This result shows that a significant molecular growth effect takes place and leads to the formation of a significant amount of large neutral species. Actually, at high C_2H_2%, acetylene fragmentation is governed by electron-impact processes that result in many competitive routes with several products, i.e. C_2H, C_2, C, CH, that, except for C_2H, do not induce molecular growth. The situation is therefore completely different as compared to the low C_2H_2% cases where C_2H_2 fragmentation is essentially insured by Ar* quenching and results in C_2H, a key-species for molecular growth.

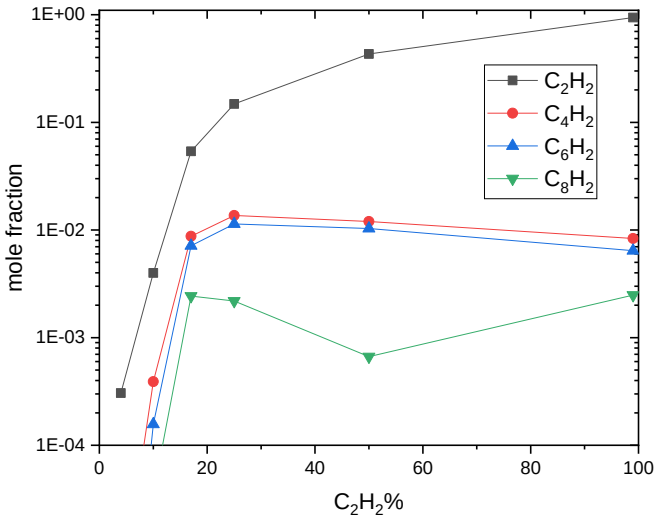

Figure 9: Molar fraction of neutral species at the center of the gap as function of acetylene in the feed gas

III. 2. Molecular growth kinetics in Ar/C2H2 plasma

a. Overall production rates of C_8 hydrocarbons

Figure 10 shows the axial profiles for the production rate of 8 carbon neutral, positive and negative species for 10% (a) and 50 % (b) acetylene percentage in the feed gas. At low C_2H_2% the major route for C_8 production involve neutral species growth processes (R1) and (R2) that take place over the entire discharge gap and show rate-values that are at least two orders of magnitude greater than those of the other routes. The C_8 production through the positive and negative channels is significant in the very narrow electronegative region located at the center of the gap where the rates of these two channels show pronounced maxima. The rate of C_8 negative ion production shows steep decrease with more than 4 orders of magnitude variation at the edge of this region. The C_8 positive ion production shows a much moderate decrease outside the electronegative region.

The situation is fairly different at large C_2H_2% in the feed gas. In this case, the major C_8 production occurs through the positive ion channel (R4). This channel remains dominant over almost all the discharge gap. The corresponding rate values are typically two orders of magnitude larger than those of neutral and negative channels, i.e., processes (R1), (R2) and (R3), in the center of the discharge. The neutral growth route remains significant over the entire discharge gap while the negative one is only effective in the narrow electronegative region.

This reaction rate analysis clearly shows that the C_6➔ C_8 molecular growth is dominated by the neutral route (R1) and (R2) at low C_2H_2% and positive ion channel (R4) at higher C_2H_2%. The negative ion route (R3) shows much smaller contribution. Further, while the C_6➔ C_8 molecular growth through neutral and positive ion channels remains effective over the entire discharge gap, the negative ion path is only active in the very narrow electronegative region.

Nevertheless, despite their interest these conclusions on the C_6➔ C_8 growth kinetics do not give any indication, and may be even misleading, as far as the estimation of the different growth channel contributions to the nucleation process is concerned. As a matter of fact, the nucleation process

takes place as a result of molecular growth over a very large size range. Therefore the contribution of a given channel (neutral, positive or negative) to the nucleation kinetic cannot be inferred from the only C_6➔ C_8 and depends on the evolution of the cluster concentration as function of the size, i.e., on the shape of the cluster size distribution at large size values. A channel characterized by a strong decrease of the corresponding cluster, i.e. neutral, positive or negative, concentration with the size will probably show a moderate or negligible contribution to the nucleation kinetics. On the opposite, a channel that maintains significant concentrations for very large cluster size is likely to significantly contribute to the nucleation kinetic. The behavior of molecular size distributions over a large size range as function of the feed gas composition will be discussed in the next sub-section

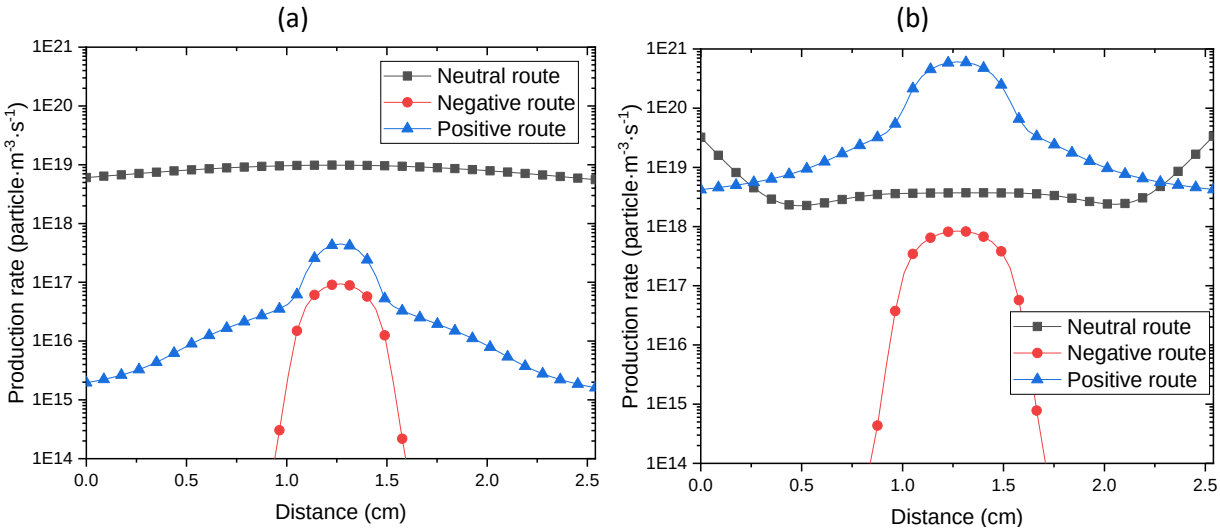

Figure 10: C_6➔C_8 growth rate for the different molecular growth routes at 10% (a) and 50% (b) acetylene percentage in the feed gas

b. Detailed size distribution of large hydrocarbons over the size range 2n=2-20.

To investigate how the neutral, positive and negative clusters concentrations evolve with their sizes, we performed simulations taking into account molecular growth up to 20 carbon atoms using the large characteristic time module. The discharge characteristics used in these simulations are those obtained by the self-consistent model taking into account up to 8-carbons species. The size distribution of neutral, positive and negative obtained are shown in figure 11 (a) and 11 (b) for 10% and 50% of C_2H_2 in the feed gas, respectively. We clearly see that neutral, negative and positive species concentration show strong exponential decreases with the size for 10% acetylene in the feed gas (figure 11(a)). This decrease is driven by the loss of a large fraction of the neutral molecules at the electrode surface and will be discussed in details in the next section. The calculated size distributions show that none of the three molecular growth channels can explain the nucleation of nanoparticles under low C_2H_2% in the frame of this model. In fact, in this case, surface deposition on the electrode limits the growth of the neutral species that are the driver for the nucleation process at low C_2H_2% in the feed gas. It is however worthy to mention that the net loss of neutrals at the electrode surface is probably significantly overestimated in the present model. As a matter of fact, more complex surface reactions such as sputtering and etching, which results in the emission of HC molecules from the deposited film are not taken into account. We believe that these processes and reactions will probably significantly reduce the net loss of HC species at the surface which would

result in an enhanced molecular growth and nucleation as compared with what is predicted by the present model that makes use of a very simple surface chemistry model.

The cluster size distributions obtained for 50% acetylene in the feed gas (figure 11 (b)) shows very different behaviors. First, the neutral cluster densities show much slower decrease with the size. This decrease even tends to be dumped with an increasing cluster size. For instance, the cluster size distribution decreases by less than one order of magnitude between C_8 and C_{18}. As a result, 18-Carbon neutral cluster shows a large density, i.e., of the order of 10^{11}-$10^{12}cm^{-3}$. Also, the negative ions density is constant as function of the cluster size with a value of few $10^{8}cm^{-3}$. This means that although the negative ions density is much lower than the neutral one in the investigated size range, the negative ions are able to preserve a constant density over very large size range and may therefore significantly contribute to the nucleation process. As matter of fact, using an extrapolation of cluster density evolutions depicted in figure 11(b) to larger sizes, one can estimate equal negative and neutral density for cluster size of C_{38}. Note however that the molecular growth of charged cluster is effective only in the narrow electronegative region of the discharge while neutral molecule growth takes place in the entire gap. The size distribution of positive ions shows a very slight decrease and varies by less than a factor 5 in the size range of 6-18 carbon atoms. In this size range, negative and positive ions mole fractions are comparable. However, extrapolating the size distribution for a larger range one can estimates positive ions concentration that are 2 order of magnitude below the negative one for C_{38}.

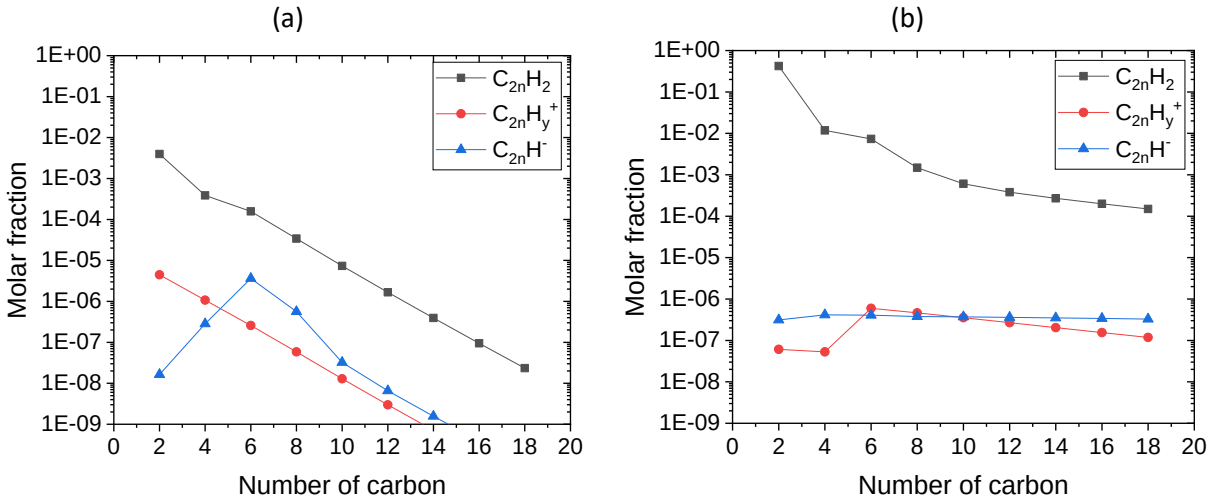

Figure 11: Molar fraction for neutral, negative and positive ions in the bulk as function of their carbon number at 10% (a) and 50% (b) of acetylene in the feed gas

It appears therefore that one may distinguish two situations as far as discharge and molecular growth processes in argon/acetylene CCRF plasmas are concerned. The first situation corresponds to cases where acetylene is highly converted and its concentration in the gap very low as compared to the feed gas. In this case, the discharge is sustained by Ar* Penning ionization, the molecular growth is driven by neutral species and the nucleation, as inferred from the present model, is unlikely. The second situation corresponds to cases where acetylene is moderately converted and its concentration in the gap significant and of the same order as in the feed gas. In this case, the discharge is sustained by electron-impact ionization of acetylene; molecular growth is driven by positive ions and leads, through recombination processes, to neutral polyynes as the major large molecular structures with significant concentrations in the gap. The cluster size distribution shows that gas phase nucleation is very likely in these conditions.

c. Interpretation of the obtained molecular size distributions in terms of large cluster kinetics

In order to understand the cluster size distributions discussed in the previous section and to identify the molecular growth path responsible for the particle nucleation at 50% of acetylene in the feed gas, i.e. large acetylene concentration in the gap, we performed a rate analysis of the different processes involved in C_{2n}->C_{2n+2} growth kinetics. Below we illustrate this analysis in the case of C_{12}➔C_{14} growth. Figure 12 shows the major consumption routes of $C_{12}H_2$, especially those processes that are involved in the molecular growth of neutral species at this gas composition. It appears that 9% of the $C_{12}H_2$ are lost with the gas flow pumped out from the reactor, wall deposition accounting for only 2% of the losses. Only 5% of $C_{12}H_2$ undergo molecular growth. The neutral molecular growth involves a direct route where C_2H attaches to $C_{12}H_2$, i.e., process (R2), and a two-step ionization/dissociative recombination route that ends-up with the production of $C_{12}H$ and its growth by reaction with C_2H_2, i.e., process (R1). The most important conclusion of this analysis, as far as the nucleation mechanism is concerned, is that the neutral size distribution shown in figure 11(b) is not consistent with a neutral cluster kinetics that is only controlled by neutral molecular growth process. As a matter of fact, the low fraction of $C_{12}H_2$ that undergoes molecular growth should have resulted in a much stronger decrease of the neutral cluster population with the size if neutral kinetics was dominant. Consequently, other processes involving charged species should be invoked to explain the fairly low decrease in the neutral size distribution and the resulting significant neutral population at large size.

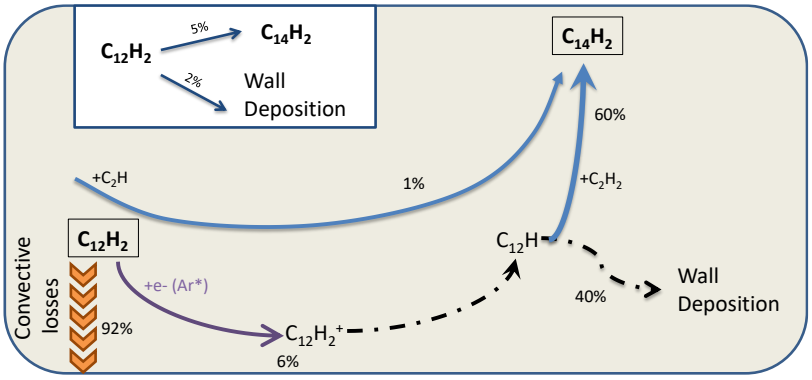

Figure 12: neutral growth route from $C_{12}H_2$ to $C_{14}H_2$ for 50% C_2H_2 in the feed gas. The number on each arrow represents the consumption fraction of the corresponding left species. Plain arrows represent volume processes while dotted arrows represent surface processes. The insert shows the fractions of the $C_{12}H_2$ contributing to molecular growth and lost at the electrode surface.

As for positive ions, two major species can be produced: $C_{12}H_2^+$ and $C_{12}H_6^+$. $C_{12}H_2^+$ is mainly produced by electron-impact, consumed by wall recombination and does not contribute to the growth process (Figure 12). This is not the case of $C_{12}H_6^+$ that, as may be seen in Figure 13, shows two major consumption routes. These are the molecular growth reaction with C_2H_2 that leads to $C_{14}H_6^+$ and the heterogeneous surface recombination. The later accounts for 26% of the ion loss and is responsible for the enhanced production of large size neutral molecules thus explaining the neutral size distributions shown in Figure 11(b). Also, the large fraction of $C_{12}H_6^+$ that undergoes molecular

growth is consistent with the slowly decreasing positive size distribution and the subsequent significant population for large positive ions (cf. Figure 11(b)).

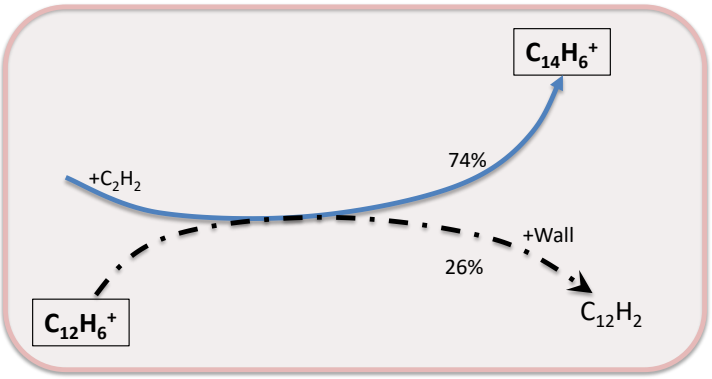

Figure 13: positive ion growth route from $C_{12}H_6^+$ to $C_{14}H_6^+$. The number on each arrow represents the consumption percentage of the corresponding left species. Plain arrows represent volume processes while dotted arrows represent surface processes.

Figure 14 shows the two major processes involved in the kinetics of $C_{12}H^-$ at 50% of C_2H_2. The first one is a molecular growth process involving C_2H_2 addition reaction ($C_{10}H^- \rightarrow C_{12}H^- \rightarrow C_{14}H^-$, blue arrow). The second one is a dynamic equilibrium between the neutrals $C_{12}H/C_{12}H_2$ and $C_{12}H^-$. This equilibrium involves radiative and dissociative attachments on one hand, and mutual recombination on the other hand (red bold arrow). A rate analysis of these processes shows that 74% of $C_{12}H^-$ experience molecular growth to $C_{14}H^-$ while the remaining 25% are lost by mutual neutralization with positive ions thus contributing to the enhanced production of large neutral species.

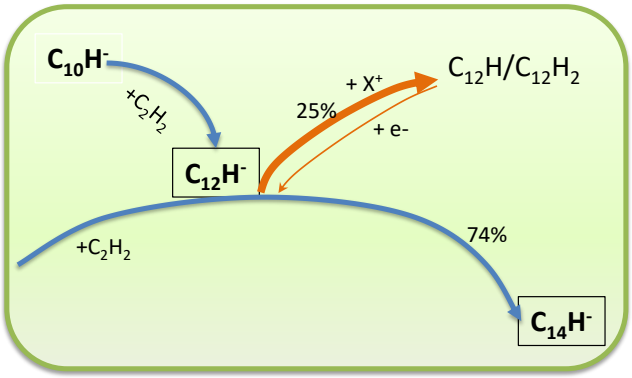

Figure 14: negative ion growth route from $C_{12}H^-$ to $C_{14}H^-$. The numbers represent the consumption fraction of the left species.

Figure15 shows an overview of the molecular growth from 10- to 14- carbon containing molecules through neutral, positive and negative growth channels. The figure particularly shows the significant coupling between positive and neutral channels through surface recombination processes. In fact, this process represents the major production channel of large neutral species and fully governs their size distributions. It is therefore responsible for the large neutral cluster densities observed in Figure 11(b). In spite of this the neutral species are not the drivers for the molecular growth. The

contribution of negative ions also remains very weak and limited to a very narrow region in the center of the gap. In fact, the molecular growth essentially takes place through the positive ion channel, i.e., process (R4), which contributes to more than 97% of C_{14} production.

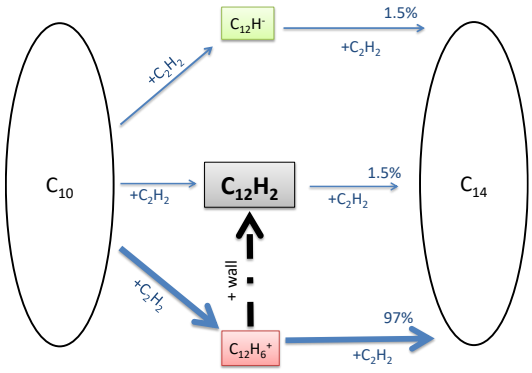

Figure15: Overview of the competition between the different processes involved in the kinetics of $C_{12}H_2$ and that compete molecular growth kinetics.

d. Sensitivity of the molecular growth to the assumption made on the interaction of the ions with the electrode

The results obtained in the previous section show that ion are responsible for the molecular growth through process (R4) even if their densities are moderate. Their recombination at the electrode surface is responsible for the observed neutral size distributions that are usually used to interpret the molecular growth mechanisms. We analyze in this section the impact that the assumption made on the ion recombination may have on the size distributions and on the molecular growth mechanism. The ions are usually assumed to fully interact with the electrode surfaces. However, two kinds of interactions are generally assumed for molecular ions. The first one, used here, assumes that ions undergo dissociative recombination that results in the emission of two neutral species, e.g., $C_{2n}H_2^+ \rightarrow C_{2n}H + H$. The second one, that was largely used in the literature [12], assumes that the ions are adsorbed by the electrodes where they fully contribute to a hydrogenated carbon film deposition process [24]. Of course these two assumptions correspond to very specific situations since the interaction of molecular ions with electrodes may be a fairly complex process that involves recombination, fragmentation, implantation and sputtering. Taking into account all these processes is out of the scope of the present work. Nevertheless, in order to investigate how the molecular growth process is sensitive to the ion-surface interaction that seems to play an important role in the gas phase molecular growth mechanism, we compared the two asymptotic situations of full dissociative recombination and a total deposition of the ions at the surface. Figure 16 shows the cluster size distribution obtained assuming that the ions are totally deposited at the surface. Comparison of these distributions with those presented in figure 11 shows that, at low C_2H_2%, the HC populations obtained assuming a full ion deposition are much lower than those obtained with a total dissociative recombination. Further the size distribution shows much stepper decrease (7 orders of magnitude) in this case, which means that the molecular growth is strongly quenched. This quenching is due to the fact that assuming full adsorption at the electrode prevents the production of neutral radicals that contribute significantly to the molecular growth through (R1) and (R2) in this discharge condition. The large decrease of positive ion densities observed when assuming full ion recombination at the electrode is due to a decrease of i) C_2H_2 concentration in the gap and ii) the

primary small ions (i.e. $C_2H_2^+$ and $C_4H_2^+$) that launch the positive ion growth channel (R3). The decrease in acetylene concentration is a direct consequence of the absence of $C_2H_2^+$ dissociative recombination. Indeed, this latter provides large amount of C_2H in the plasma which results in enhanced C_2H_2 production through surface recombination at the electrodes. This decrease in the acetylene concentration also explains the decrease of the primary positive ions.

For 50% C_2H_2% in the feed gas, the positive and negative ion distributions obtained assuming either dissociative recombination or total adsorption of positive ions at the electrode are very similar. However, a strong difference is observed on neutral species size distributions. This shows strong decrease, almost two orders of magnitude, especially for molecules with more than 6-Carbons, when full ion adsorption is assumed. These results may be easily explained since large neutral production is fully governed by positive ions recombination at the electrode when this process is taken into account. This change in the size distribution does not affect the molecular growth kinetics since this latter takes place essentially through positive ions the kinetics of which is not sensitive to these boundary conditions that make use of the same value for the ion loss coefficient. It is worthy to mention here that despite its decrease, the concentration of large neutral polyynes remains fairly high with a density value in the range 10^{11}-10^{12} cm^{-3}, which is likely to insure a significant nucleation.

The nature of the boundary conditions adopted in these simulations also affects the mass of carbon transferred from the gas phase to the hydrogenated carbon film growing at the electrodes. The total mass flux density transferred to the film is approximately $6x10^{-7}$ $kg{\cdot}m^{-2}{\cdot}s^{-1}$, 80% of which is due to positive ions sticking, when full ion-sticking boundary conditions are assumed. This is just 4 times larger than the total mass flux density value obtained when a full dissociative recombination is assumed for positive ions and only radicals can stick to the film. It appears therefore that the effect of the boundary conditions on the total mass flux density transferred to the film is surprisingly moderate. This is due to a compensation effect between positive and HC radical fluxes at the surface. As a matter of fact, when full ion sticking is assumed, the mass transfer due to ions is strongly enhanced. Simultaneously, the $C_{2n}H$ radical concentration and the corresponding mass transfer significantly decrease as compared to a full ion recombination boundary condition.

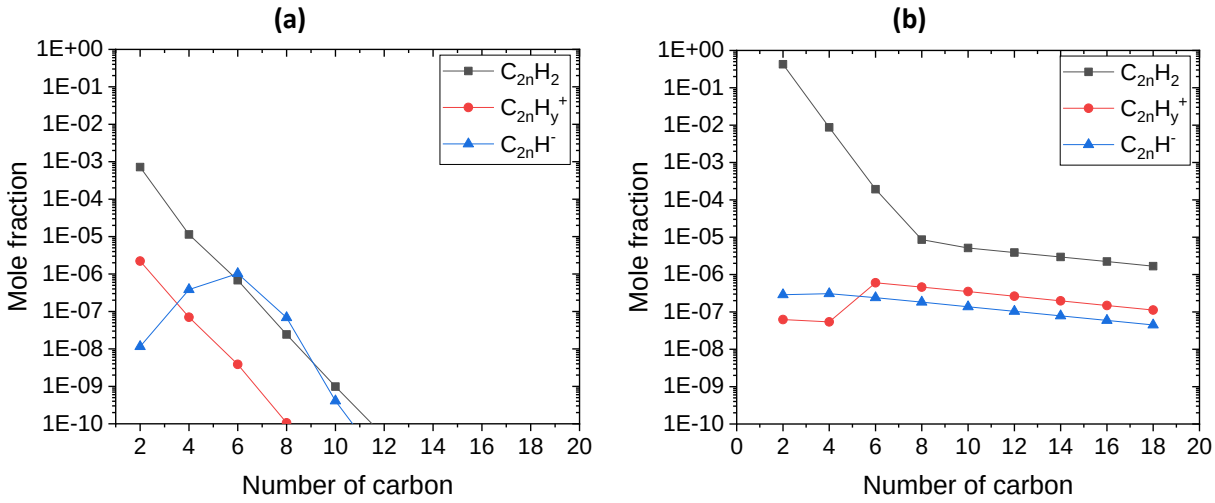

Figure 16: size distributions of neutral, negative and positive ions calculated at the center of the gap assuming a full adsorption of positive ions at the electrodes forC_2H_2% of 10% (a) and 50% (b)

IV. Conclusion

In this paper we presented a modeling study of molecular growth processes taking place in argon-acetylene plasmas. The model takes into account the coupling between the discharge dynamics, the plasma kinetics, including molecular growth processes and large hydrocarbon chemistry, and gas flow effect. We essentially made use of the molecular growth model proposed in [24] and [14]. We mainly focused on the identification of the key-precursors and processes that are likely to be responsible for the gas phase nucleation of dust particles for different acetylene concentrations in the feed gas. We showed that for the discharge conditions considered in this work, i.e., p=10 Pa, V_{RF}=100 V and gap distance=2.5 cm, two situations may be distinguished.

A first one corresponds to discharge conditions where acetylene conversion is high and lead to low C_2H_2 concentration in the gap. In this case, the molecular growth is driven by neutral species through process (R1) and (R2). The large neutral molecules are much more populated than the corresponding positive and negative ions in this case. Nevertheless, the size distribution of these species show very strong decrease for large polyyne molecules which prevent nucleation through neutral species. As a result, the molecular growth model along with the simplified surface chemistry used in this study cannot explain the observed dust particles production under low acetylene concentration. A possible explanation would be the importance of a complex surface processes not taken into account in the present model, i.e., sputtering and etching of the hydrogenated carbon deposit, that may affect the gas phase composition and enhance the gas phase molecular growth.

The second situation corresponds to limited acetylene conversion yield and a large acetylene concentration in the gap. In this case, the molecular growth process is driven by positive ions, i.e., process (R4). The size distributions of large molecular hydrocarbons show very slight decrease for neutrals and positively charged ions and an almost no variation for negative ions. This shows that the molecular growth model used in this work can fully explain the gas phase dust particle nucleation under high acetylene concentration in the feed gas, i.e., C_2H_2% greater than 20%. An important point revealed in the present study is that even though the nucleation is driven by positive ions, the large polyynes are mainly neutral. This is due to the fast dissociative recombination of large ions on the electrode surface.

A study of the sensitivity of the molecular growth kinetics to the boundary conditions adopted for the large molecular ions showed that even if these ions are assumed to be fully absorbed at the electrodes, they still insure a significant molecular growth and nucleation kinetics. In any case, the results obtained here are consistent with experimental studies showing that dust particle formation in hydrocarbon plasma may be very sensitive to the electrode surface and reactor wall conditioning [46]. This clearly emphasizes that an improved molecular growth and nucleation model should take into account a much more detailed surface model. In particular, the impact of sputtering and etching of the hydrogenated carbon films that form on the electrode in hydrocarbon containing plasmas on the composition of the gas phase should be included in the model. This line of improvement is the subject of a current research effort.

Acknowledgements

This work was partly supported by the French National Research Agency (ANR) through the MONA project (ANR-18-CE30-0016). One of us (KH) is grateful to Institut Universitaire de France for its support.

References

[1] A. Varade, A. Krishna, K.N. Reddy, M. Chellamalai, P.V. Shashikumar, in: S. Narendranath, M.R. Ramesh, D. Chakradhar, M. Doddamani, S. Bontha (Eds.), International Conference on Advances in Manufacturing and Materials Engineering, 2014, pp. 1015-1019.

[2] M. Weiler, S. Sattel, T. Giessen, K. Jung, H. Ehrhardt, V. Veerasamy, J. Robertson, Physical Review B 53 (1996) 1594.

[3] S. Vasquez-Borucki, W. Jacob, C.A. Achete, Diamond and Related Materials 9 (2000) 1971-1978.

[4] L. Liu, A. Das, C.M. Megaridis, Carbon 69 (2014) 1-16.

[5] B. Kasinathan, R.M. Zawawi, Carbon-based Nanomaterials for Drugs Sensing: A Review, Trans Tech Publ, 2015, 13-39.

[6] S. Nissen, J. Heeg, M. Warkentin, D. Behrend, M. Wienecke, Surface & Coatings Technology 316 (2017) 180-189.

[7] R.W. Poon, J.P. Ho, X. Liu, C. Chung, P.K. Chu, K.W. Yeung, W.W. Lu, K.M. Cheung, Nuclear Instruments and Methods in Physics Research Section B: Beam Interactions with Materials and Atoms 237 (2005) 411-416.

[8] A. Grill, B. Meyerson, V. Patel, J. Reimer, M. Petrich, Journal of Applied Physics 61 (1987) 2874-2877.

[9] E. Kovacevic, J. Berndt, T. Strunskus, L. Boufendi, Journal of Applied Physics 112 (2012).

[10] J.R. Doyle, Journal of applied physics 82 (1997) 4763-4771.

[11] S. Stoykov, C. Eggs, U. Kortshagen, Journal of Physics D: Applied Physics 34 (2001) 2160.

[12] K. De Bleecker, A. Bogaerts, W. Goedheer, Physical Review E 73 (2006) 026405.

[13] K. De Bleecker, A. Bogaerts, W. Goedheer, New Journal of Physics 8 (2006) 178.

[14] M. Mao, J. Benedikt, A. Consoli, A. Bogaerts, Journal of Physics D: Applied Physics 41 (2008) 225201.

[15] A. Akhoundi, G. Foroutan, Physics of Plasmas 24 (2018) 053516.

[16] I. Stefanović, N. Sadeghi, J. Winter, B. Sikimić, Plasma Sources Science and Technology 26 (2017) 065014.

[17] I. Schweigert, A. Alexandrov, D. Ariskin, F. Peeters, I. Stefanović, E. Kovačević, J. Berndt, J. Winter, Physical Review E 78 (2008) 026410.

[18] D. Ariskin, I. Schweigert, A. Alexandrov, A. Bogaerts, F. Peeters, Journal of applied physics 105 (2009) 063305.

[19] I.B. Denysenko, E. von Wahl, S. Labidi, M. Mikikian, H. Kersten, T. Gibert, E. Kovačević, N.A. Azarenkov, Plasma Physics and Controlled Fusion 61 (2019) 014014.

[20] I. Denysenko, E. von Wahl, M. Mikikian, J. Berndt, S. Ivko, H. Kersten, E. Kovacevic, N. Azarenkov, Journal of Physics D: Applied Physics 53 (2020) 135203.

[21] J. Lin, S. Orazbayev, M. Hénault, T. Lecas, K. Takahashi, L. Boufendi, Journal of Applied Physics 122 (2017) 163302.

[22] U. Bhandarkar, M. Swihart, S. Girshick, U. Kortshagen, Journal of Physics D: Applied Physics 33 (2000) 2731.

[23] B. Annemie, E. Maxie, M. Ming, N. Erik, Journal of Physics D: Applied Physics 44 (2011) 174030.

[24] G. Tetard, A. Michau, S. Prasanna, J. Mougenot, P. Brault, K. Hassouni, Plasma Sources Science and Technology 30 (2021) 105015.

[25] M. Coltrin, R. J. Kee, G. H. Evans, Journal of The Electrochemical Society 136 (1989) 819-829.

[26] C. Deschenaux, A. Affolter, D. Magni, C. Hollenstein, P. Fayet, Journal of Physics D: Applied Physics 32 (1999) 1876.

[27] I. Denysenko, E. Von Wahl, S. Labidi, M. Mikikian, H. Kersten, T. Gibert, E. Kovačević, N. Azarenkov, Plasma Physics and Controlled Fusion 61 (2018) 014014.

[28] D. Herrebout, A. Bogaerts, R. Gijbels, W.J. Goedheer, A. Vanhulsel, IEEE transactions on plasma science 31 (2003) 659-664.

[29] M. Frenklach, A.M. Mebel, Physical Chemistry Chemical Physics 22 (2020) 5314-5331.
[30] K. Hassouni, F. Mohasseb, F. Bénédic, G. Lombardi, A. Gicquel, Pure and applied chemistry 78 (2006) 1127-1146.
[31] Biagi, Database, www.lxcat.net, 2021.
[32] D. Reiter, R. Janev, Contributions to Plasma Physics 50 (2010) 986-1013.
[33] W. Hwang, Y.K. Kim, M.E. Rudd, The Journal of Chemical Physics 104 (1996) 2956-2966.
[34] M. Frenklach, H. Wang, Physical Review B 43 (1991) 1520.
[35] J. Perrin, C. Bohm, R. Etemadi, A. Lloret, Plasma Sources Science and Technology 3 (1994) 252.
[36] J. Knight, C. Freeman, M. McEwan, V. Anicich, W. Huntress, Journal of Physical Chemistry 91 (1987) 3898-3902.
[37] F. Carelli, M. Satta, T. Grassi, F. Gianturco, The Astrophysical Journal 774 (2013) 97.
[38] A. Hickman, The Journal of Chemical Physics 70 (1979) 4872-4878.
[39] A. Von Keudell, C. Hopf, T. Schwarz-Selinger, W. Jacob, Nuclear Fusion 39 (1999) 1451.
[40] E. Gogolides, H.H. Sawin, Journal of Applied Physics 72 (1992) 3971-3987.
[41] K. Hassouni, F. Silva, A. Gicquel, Journal of Physics D: Applied Physics 43 (2010) 153001.
[42] M. Cazalilla, N. Lorente, R.D. Muino, J.-P. Gauyacq, D. Teillet-Billy, P. Echenique, Physical Review B 58 (1998) 13991.
[43] A.-P. Herrendorf, V. Sushkov, R. Hippler, Journal of Applied Physics 121 (2017) 123303.
[44] A. Baby, C.M.O. Mahony, P.D. Maguire, Plasma Sources Science and Technology 20 (2011) 015003.
[45] I.B. Denysenko, E. von Wahl, S. Labidi, M. Mikikian, H. Kersten, T. Gibert, Plasma Processes and Polymers 16 (2019) 1800209.
[46] I. Géraud-Grenier, M. Mikikian, F. Faubert, V. Massereau-Guilbaud, Journal of Applied Physics 126 (2019) 063301.